RESEARCH ARTICLE

Evaluating Enthalpy Production in Geothermal Reservoirs: Insights from Response Surface Methodology and Advanced Machine Learning Techniques

Eric Thompson Brantson[1,*], **Stephen Dwamena Akoto Obeng**[1], **Daniel Ocran**[1], **Emmanuel Karikari Duodu**[2], **Zainab Ololade Iyiola**[3], **Eugene Jerry Adjei**[1], **Joel Adu-Awuku**[1] **and Adu Gyamfi Owusu**[1]

[1] Department of Petroleum and Natural Gas Engineering, School of Petroleum Studies, University of Mines and Technology, Tarkwa, Ghana
[2] School of Energy Resources, China University of Geosciences Beijing, Beijing 100083, China
[3] Mewbourne School of Petroleum and Geological Engineering, University of Oklahoma, Norman, OK 73019, United States

Abstract

Enthalpy is a key thermodynamic parameter governing energy extraction efficiency in Enhanced Geothermal Systems (EGS). Although Machine Learning (ML) has been widely applied in geothermal modeling, few studies have systematically integrated Response Surface Methodology (RSM) with ML to develop and compare multiple predictive models for enthalpy production. Using datasets from CMG STARS simulations, we developed predictive models based on RSM and four ML techniques (Random Forest, Decision Tree, XGBoost, and Support Vector Machine). A Central Composite Design (CCD) in CMG CMOST established relationships between operational parameters and enthalpy, while Particle Swarm Optimization (PSO) determined the optimal operating conditions within the investigated design space. The RSM model achieved an R^2 of 0.999404, outperforming Random Forest (0.9929), Decision Tree (0.9882), XGBoost (0.9883), and Support Vector Machine (0.9888). PSO optimization yielded a maximum cumulative enthalpy of 4.507×10^{16} J. These results demonstrate that integrating RSM with ML provides accurate and robust predictive capability with efficient optimization of geothermal reservoir performance. This study offers a structured framework combining statistical and data-driven approaches to improve geothermal energy assessment and decision-making.

Keywords: geothermal reservoir, response surface

Submitted: 06 February 2026
Revised: 19 April 2026
Accepted: 21 April 2026
Published: 30 April 2026

Vol. 2, **No.** 2, 2026.
10.62762/RS.2026.366192

***Corresponding author:**
✉ Eric Thompson Brantson
etbrantson@umat.edu.gh

Citation
Brantson, E. T., Obeng, S. D. A., Ocran, D., Duodu, E. K., Iyiola, Z. O., Adjei, E. J., Adu-Awuku, J., & Owusu, A. G. (2026). Evaluating Enthalpy Production in Geothermal Reservoirs: Insights from Response Surface Methodology and Advanced Machine Learning Techniques. *Reservoir Science*, 2(2), 151–171.

methodology, enthalpy prediction, particle swarm optimization, enhanced geothermal system.

1 Introduction

In the face of escalating global warming and climate change, the need to rapidly transition from fossil fuels to renewable and clean energy sources becomes increasingly pressing [1]. Geothermal energy, as an environmentally friendly and sustainable resource, is increasingly recognized for its potential applications in diverse fields such as space heating systems, electricity generation and industrial greenhouse cultivation [2]. Unlike some other renewable sources such as wind and solar energy, geothermal energy stands out due to its efficiency and year-round availability, unaffected by weather conditions or seasonal fluctuations [2, 3].

The growing interest in geothermal energy is reshaping the energy landscape, addressing carbon reduction goals, and contributing to energy security in the context of climate change [2, 4]. Despite its promising attributes, there still exists a significant level of uncertainty in terms of energy recovery and assessment in geothermal systems. This underscores the need for contemporary data-driven models to improve our current understanding and optimize the use of this valuable resource.

The effectiveness of geothermal reservoir heat extraction is largely determined by the interaction between fractures and the rock matrix during fluid flow [5]. The pattern of fluid movement in geothermal reservoirs is strongly influenced by temperature changes within the rock matrix, caused by the injection of cold water into fractures [5, 6]. This injection process generates thermal stress and strain in the matrix, leading to either compaction or expansion of the pore space of the reservoir. Current research on geothermal reservoir heat energy recovery is primarily focused on reservoir development and maximization of heat energy production [4, 7]. Hydraulic fracturing, a technique adopted from the oil and gas industry, is widely used to enhance geothermal reservoirs. These fractures act as channels for fluid movement, promoting heat generation within the reservoir. After hydraulic fracturing, heat is extracted from the stimulated geothermal reservoir by pumping in cold fluid [8]. To efficiently harness high-temperature heat from the rock matrix, it is crucial to ensure that the injected fluid remains in the reservoir for a sufficient period, while maintaining a high flow rate throughout an extended production phase [7, 9]. Achieving this goal requires the development of an optimal production strategy that considers the dynamics in the properties of the rock and fluid during operation.

In recent decades, Machine Learning (ML) has emerged as an essential modeling tool in the study of geothermal systems. ML assists in selecting input parameters and assessing their sensitivity. Its predictive capacity surpasses traditional methods, due to its versatile structure and robust ability to retain historical data [20, 21]. This inherent characteristic provides ML with exceptional capabilities to make universal predictions tailored to specific responses [20, 22]. However, Response Surface Methodology (RSM) is a commonly used predictive modeling technique that employs statistical methods to evaluate the influence of experimental variables and their interactions on particular outcomes [23]. Central Composite Design (CCD) is one of the most commonly used response surface techniques, offering significant optimization benefits for many processes [24]. RSM is particularly advantageous over other predictive methods due to its capacity to work efficiently with limited experimental data [23, 25]. Furthermore, RSM facilitates the creation of graphical response surface models, including curvature, and supports analysis of variance, enhancing the potential for process optimization. However, it is important to recognize that RSM's predictive and optimization capabilities are inherently constrained within the boundaries of operational conditions, making it challenging to extend process understanding beyond these limits [23, 25]. In recent years, ML has generated significant interest across a wide spectrum of geoscience applications [22, 26–29], and its integration with renewable energy systems has been widely explored [30]. ML algorithms have shown effectiveness in various tasks such as regression, prediction, and function approximation. These techniques have been successfully applied in the prediction of rock and fluid properties, the identification of lithofacies, the forecasting of well production, and other management operations [26, 28, 29]. Machine learning models are capable of addressing complex problems with reduced computational overhead while maintaining high accuracy in handling nonlinear relationships [21, 26]. Researchers have been interested in implementing ML models in geothermal systems in recent times [31, 32].

In the domain of geothermal research, the use of machine learning and deep learning algorithms has been pivotal for various applications. Jiang et al. [10] demonstrated the estimation of enhanced

geothermal reservoir energy production using a recurrent neural network (RNN) as a data-driven alternative to complex simulation models. He et al. [1] also harnessed ML algorithms, utilizing eight geological features as input data to predict geothermal heat flow. Assouline et al. [11] employed a supervised approach to estimate temperature maps at shallow depths. Tut Haklidir and Haklidir [43] applied a machine learning approach to predict reservoir temperatures in the western Anatolia geothermal systems of Turkey, utilizing hydrogeochemical data as input features. In their efforts to accurately assess deep temperature fields, Spichak et al. [13] and Ishitsuka et al. [14] used neural networks trained on resistivity data. Their findings demonstrated a significant enhancement in the accuracy of the estimation caused by the application of machine learning algorithms. Rezvanbehbahani et al. [12] focused on estimating geothermal heat flux, drawing on a comprehensive set of pertinent geological features and global measurements. Gudmundsdottir et al. [31] and Siler et al. [42] employed unsupervised methods to identify critical factors impacting geothermal production, utilizing datasets on geologic factors and tracer response data, respectively. Using ML techniques and neural networks, Holtzman et al. [40] revealed cyclic changes in seismic source spectra in the Geysers geothermal field, while Zheng et al. [41] successfully characterized small-scale faults and fractures by analyzing microseismic data. The ongoing development of these ML models holds promise for the creation of more accurate subsurface structural models. This progress is poised to significantly impact geothermal research and its practical applications. Maharsi et al. [15] employed RSM to construct a predictive model for thermal power extraction from liquid-dominated geothermal reservoirs. The model incorporated geothermal reservoir parameters such as reservoir temperature, conductivity, porosity, and permeability as input variables to identify the factors that exert the most significant influence on thermal power generation. Sutopo et al. [16] conducted a numerical simulation technique to evaluate the resource potential of the Karaha–Talaga Bodas geothermal field and to forecast the behavior of the reservoir under various development scenarios. Their research investigated the effectiveness of an experimental design and RSM in addressing the inherent uncertainties associated with geothermal reservoir modeling, leading to the assessment of probabilistic resources. Wang et al. [17] utilized Experimental Design (ED) and RSM to evaluate the potential thermal energy in a research area within the Maichen Sag, a promising geothermal prospect in South China. This probabilistic assessment approach effectively incorporated uncertainty and risk factors into the evaluation of geothermal projects, allowing a range-based quantification of the power potential. There is a notable lack of studies combining RSM with ML for predictive modeling of enthalpy production, underlining the need for further research to fully harness ML's potential in geothermal energy assessment and exploration. Despite these advancements, most studies focus on either machine

Table 1. Classification and critical comparison of existing studies on geothermal prediction models.

Category	Study	Method/Technique	Application Area	Key Strengths	Key Limitations
Machine Learning (ML)	Jiang et al. [10]	Recurrent Neural Network (RNN)	Geothermal energy production prediction	Captures temporal dynamics effectively	Requires large datasets; complex training
	He et al. [1]	Multiple ML algorithms	Geothermal heat flow prediction	High predictive accuracy	Limited interpretability
	Assouline et al. [11]	Supervised ML	Shallow temperature mapping	Good spatial prediction capability	Highly data-dependent
	Rezvanbehbahani et al. [12]	ML models	Global geothermal heat flux estimation	Handles large-scale datasets	High computational cost
	Spichak et al. [13]	Neural Networks	Deep temperature estimation	Improved estimation accuracy	Requires careful model tuning
	Ishitsuka et al. [14]	Neural Networks (Bayesian)	Subsurface temperature distribution	Handles uncertainty effectively	Computational complexity
Response Surface Methodology (RSM)	Maharsi et al. [15]	RSM	Thermal power extraction	Efficient with limited data; interpretable	Limited extrapolation capability
	Wang et al. [17]	RSM + Experimental Design	Resource assessment	Incorporates uncertainty analysis	Less flexible for nonlinear systems
	Sutopo et al. [16]	RSM + Simulation	Reservoir behavior prediction	Handles experimental uncertainty	Limited generalization
Hybrid Approaches	Gudala and Govindarajan [9]	RSM + ML + ARIMA	Reservoir modeling	Improved prediction accuracy	Limited comparative analysis
	Ye et al. [18]	RSM + Optimization	Multi-objective optimization	Effective optimization capability	Limited ML integration
Optimization Techniques	Kennedy and Eberhart [19]	Particle Swarm Optimization (PSO)	General optimization	Fast convergence; simple implementation	Depends on model quality

learning or statistical approaches independently, with limited integration between them. In addition, comprehensive comparative studies involving multiple predictive models are scarce, and optimization techniques are often not systematically incorporated. These limitations highlight the need for an integrated framework that combines statistical design, machine learning, and optimization techniques. To provide a clearer and more structured comparison of existing studies, previous research on geothermal prediction is classified and critically evaluated in Table 1, highlighting their methodologies, strengths, and limitations.

In this study, an enhanced geothermal model employing a dual-permeability model approach was simulated using a CMG STARS simulator, and then CMG CMOST based CCD experimental data were developed for predicting large-scale field cumulative enthalpy production. This model was selected for this study due to its ability to realistically simulate naturally fractured reservoirs, its improved handling of non-instantaneous matrix-fracture fluid exchange, and its enhanced ability to predict thermal recovery efficiency by considering both conduction in the matrix and convection in fractures. Therefore, this study advocates for the use of RSM and ML models as prediction tools which will also enhance the efficient full-field implementation of these techniques in reducing the uncertainty associated with geothermal resource optimization and assessment. This study, therefore, addresses these gaps by developing and evaluating predictive models using RSM and multiple machine learning techniques, followed by optimization using PSO. This integrated approach enables improved predictive accuracy, a deeper understanding of parameter interactions, and efficient identification of optimal operating conditions. The main contributions of this paper are summarized as follows:

- Build a streamlined enthalpy prediction database for geothermal reservoirs, enabling efficient uncertainty analysis.
- This study bridges the gap between RSM and ML, improving the accuracy and reliability of energy output prediction in geothermal systems.

This study is structured as follows: Section 2 outlines the methodology, including the specific ML models and RSM techniques used. The results and discussion are presented in Section 3, where the performance of various models and the efficacy of RSM in optimizing operational conditions are analyzed. Finally, Section 4 concludes the study, summarizing the key findings of the present investigation.

2 Methodology

2.1 Description of the Response Surface Methodology (RSM) Technique

The Response Surface Methodology is a collection of statistical and mathematical techniques [23]. RSM explores the relationships between input variables (parameters) and responses (objective functions). The main idea of RSM is to use a set of designed experiments to build a proxy (approximation) model to represent the original complicated reservoir simulation model as shown in Eq.(1):

$$y = a_0 + \sum_{j=1}^{k} a_j x_j + \sum_{j=1}^{k} a_{jj} x_j^2 + \sum_{i<j} a_{ij} x_i x_j \qquad (1)$$

where y = Response (objective function), a_0 = Intercept, $a_1, a_2, \ldots, a_k$ = Coefficients of linear terms, a_{jj} = Coefficients of quadratic terms, a_{ij} = Coefficients of interaction terms, and $x_1, x_2, \ldots, x_k$ = Input variables (parameters).

Parameter space sampling is an important step in sensitivity analysis and uncertainty assessment. The parameter space is usually extremely large for a given set of parameters and sample levels. For example, the number of all possible experiments (i.e., full factorial experiment) for a study with 5 parameters with 3 levels may result in $3^5 = 243$ experiments. Thus, according to statistical experimental design theory, to efficiently explore the possible parameter space, selecting the design can be performed using the following sampling methods: two-level classical experimental designs (fractional factorial and Plackett-Burman designs), three-level classical experimental designs (Box-Behnken and Central Composite Designs), and Latin hypercube design.

The CCD consists of 2^k factorial runs, $2k$ axial runs, and n_c replicated central runs (where k = number of independent variables) [23]. The merits of adopting the CCD include: (i) the central position with star points in each factorial space (i.e., $\alpha = \pm 1$); (ii) it requires fewer levels of each factor (3 levels against 5 for other designs); and (iii) it can incorporate a full factorial design with appropriate star points [23, 39]. The CCD three-level classical experimental design was used in this study as shown in Figure 1.

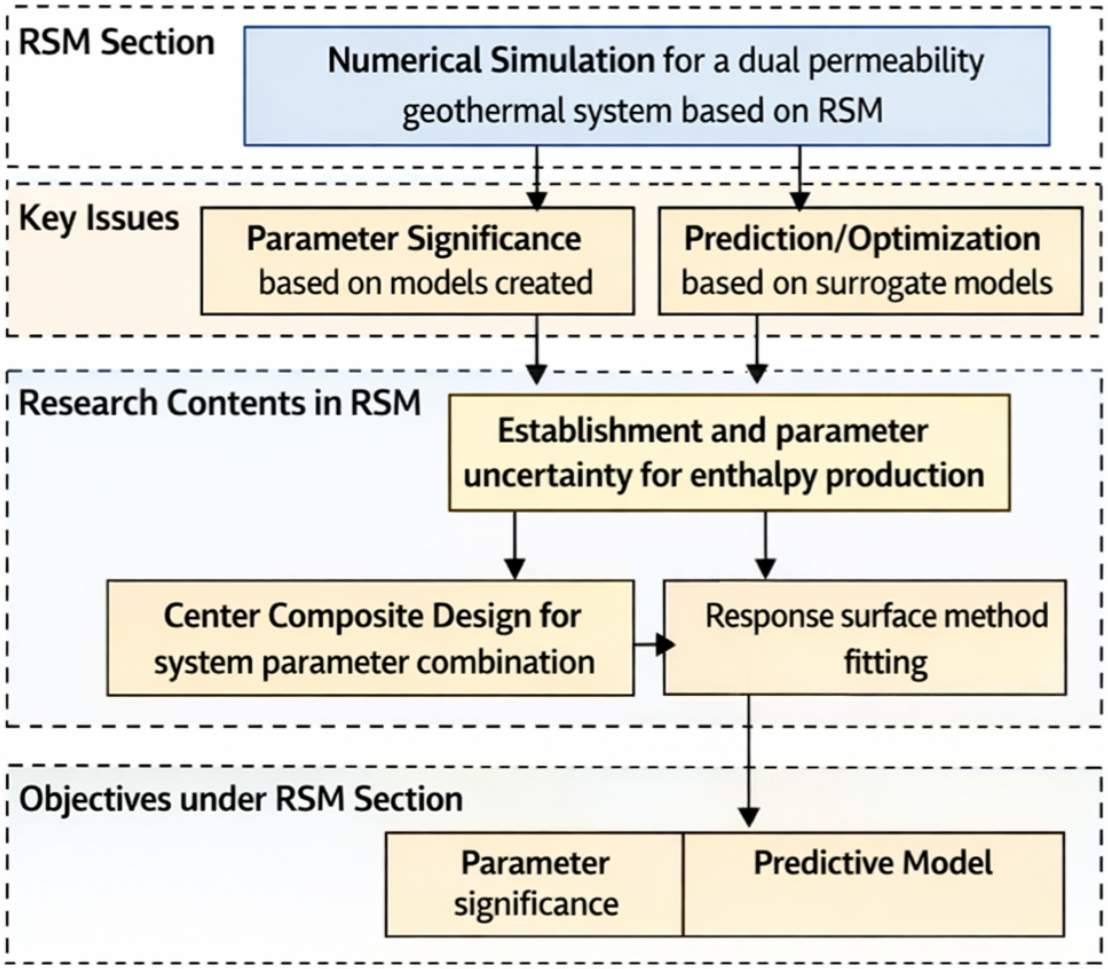

Figure 1. Developed response surface methodology procedure.

2.2 PSO Algorithm

Particle Swarm Optimization (PSO) is a population-based, stochastic optimization method that adapts over time [19]. The process starts with initializing particles and assigning them velocities. Each particle's position is evaluated using the objective function, identifying the best value and location for the function. New velocities are then computed based on the particle's current velocity, its personal best position, and the best positions of its neighbors. The particles' positions are updated iteratively by adding their velocities to their current locations, ensuring they remain within defined boundaries. This process continues until a specified stopping condition is met.

Table 2. Parameters related to the PSO model.

Parameter	Value
Inertia Weight	0.7298
Cognition Component	1.49618
Social Component	1.49618
Population size	20

In an n-dimensional search space, the position and velocity of particle j are represented by vectors $X_j = (X_{j1}, X_{j2}, \ldots, X_{jn})$ and $V_j = (V_{j1}, V_{j2}, \ldots, V_{jn})$, respectively. Let $X_{\text{pbest},j}$ be the personal best position of particle j and X_{gbest} be the global best position of the group. Figure 2 shows the developed PSO procedure, and Table 2 shows the PSO model parameters. The modified velocity and position of each particle can be calculated using the current velocity and distance from $X_{\text{pbest},j}$ and X_{gbest} as follows:

$$\begin{aligned} V_{ij}^{k+1} &= V_{ij}^{k} + C_p r_p \left(X_{\text{pbest},ij}^{k} - X_{ij}^{k} \right) \\ &+ C_g r_g \left(X_{\text{gbest},i}^{k} - X_{ij}^{k} \right) \\ i &= 1, 2, \ldots, N; \quad j = 1, 2, \ldots, p \end{aligned} \tag{2}$$

where k is the iteration count, V_{ij}^{k} is the velocity of the j-th particle of the i-th variable at the k-th iteration, X_{ij}^{k} is the position of the j-th particle of the i-th variable at the k-th iteration, C_p, C_g are the cognitive and social acceleration coefficients, N is the total number of variables, $X_{\text{pbest},ij}^{k}$ is the personal best position of the

Table 3. Comparison of the ML models: strengths and limitations.

Model	Strengths	Limitations
Random Forest	Handles large datasets well Reduces overfitting through averaging.	Can be computationally expensive May not perform well with small datasets.
Decision Tree	Simple to understand and interpret Works well with categorical and numerical data.	Prone to overfitting, especially with deep trees Sensitive to small data variations.
XGBoost	Highly flexible and powerful Handles missing data and outliers effectively.	Requires significant computational resources Hyperparameter tuning can be complex.
Support Vector Machine (SVM)	Effective for high-dimensional data Works well with non-linear relationships.	Sensitive to parameter tuning May not perform well with noisy data.

j-th particle of the i-th variable until the k-th iteration, $X^k_{\text{gbest},i}$ is the global best value of the i-th variable until the k-th iteration, and r_p, r_g are uniformly distributed random numbers.

The position update equation is

$$X_{ij}^{k+1} = X_{ij}^k + V_{ij}^{k+1} \quad i = 1, 2, \ldots, N; \quad j = 1, 2, \ldots, p \tag{3}$$

Modified velocity update with inertia weight is then defined as

$$V_{ij}^{k+1} = W \cdot V_{ij}^k + C_p r_p \left(X^k_{\text{pbest},ij} - X^k_{ij} \right) + C_g r_g \left(X^k_{\text{gbest},i} - X^k_{ij} \right) \quad i = 1, 2, \ldots, N; \quad j = 1, 2, \ldots, p \tag{4}$$

where W is the inertia weight.

2.3 Machine Learning Methods

In this section, a comprehensive summary of the ML models employed in this study is presented to estimate the production of enthalpy. Multiple algorithms were utilized for training and testing regression models, including Support Vector Machine (SVM) and decision tree-based models (e.g., Decision Tree, XGBoost, and Random Forest). In this paper, the results of the four ML algorithms and RSM are compared. These algorithms are different, and it is extremely important to properly compare their accuracies and errors. For each algorithm, the primary focus was on developing the best-performing model. This applies not only to hyperparameter tuning, but also to data preprocessing. In particular, standardization of input features was implemented for SVM. For the XGBoost, Decision Tree, and Random Forest models, no improvement was observed after standardizing the features; thus, the decision was made not to standardize the input features. Table 3 shows the comparison of the ML models' strengths and weaknesses as employed in this study. Figure 3 illustrates the ML procedure developed which has been used for this study [33].

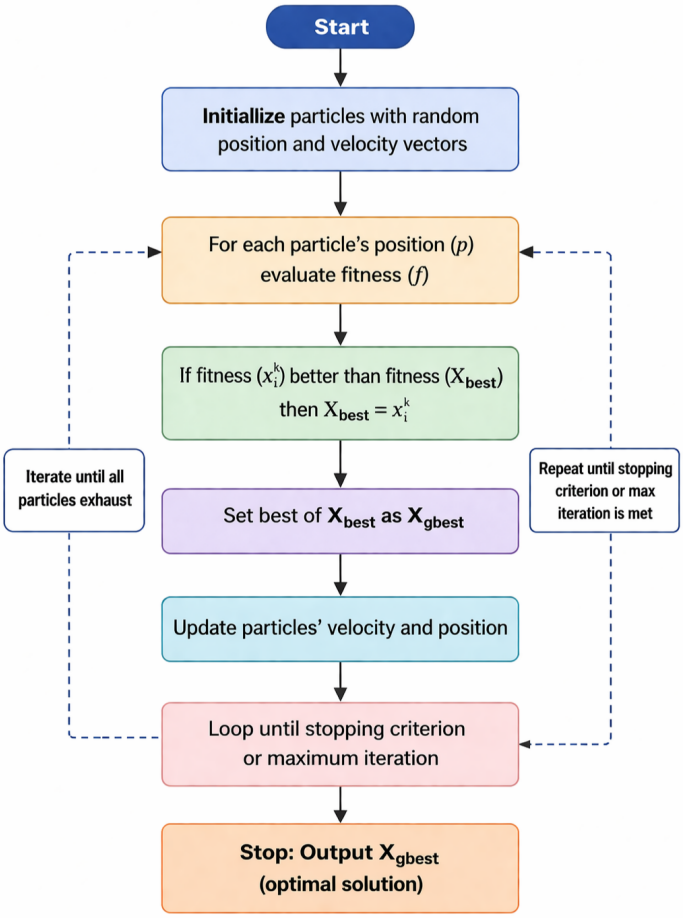

Figure 2. Developed Particle Swarm Optimization procedure.

2.3.1 *Description of the Decision Tree Regression Technique*

A decision tree is one of the most commonly used ML algorithms for solving regression as well as classification problems [29, 33]. As the name suggests, the algorithm uses a tree-like model of decisions to predict either the target value (regression) or the target class (classification). The root node represents the topmost node of the tree that represents all the data points. Decision nodes are the nodes that are further

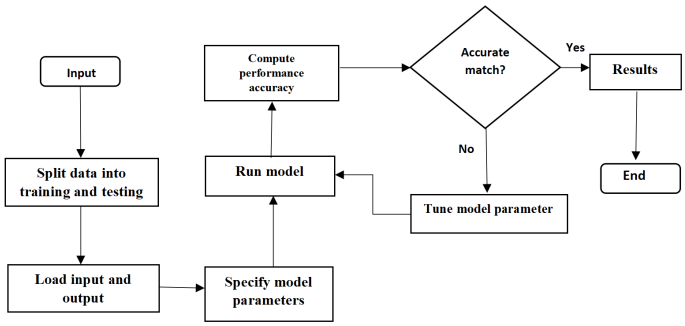

Figure 3. Developed machine learning procedure.

split into sub-nodes, i.e., this node that is split is called a decision node. Nodes that do not split are called Leaf or Terminal nodes. These nodes are often the final result of the tree.

The splitting process starts at the root node and is followed by a branched tree that finally leads to a leaf node (terminal node) that contains the prediction or the final result of the algorithm. Construction of decision trees usually works top-down, by choosing a variable at each step that best splits the set of items. Each sub-tree of the decision tree model can be represented as a binary tree where a decision node splits into two nodes based on the conditions. Decision trees in which the target variable or the terminal node can take continuous values are called regression trees. If the target variable can take a discrete set of values, these trees are called classification trees. The decision tree process is shown in Figure 4.

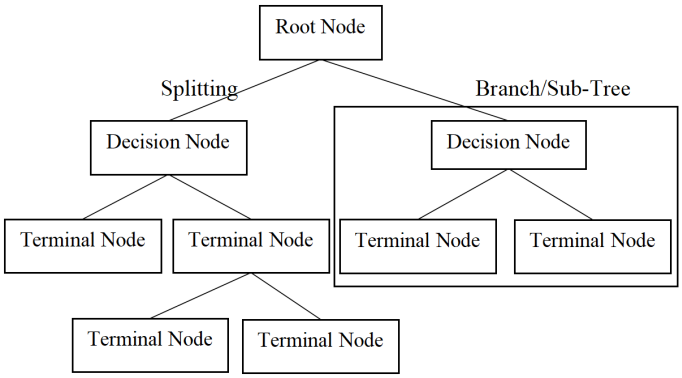

Figure 4. Decision Tree Process.

2.3.2 *Description of the Random Forest Regression Technique*

The Random Forest technique is a powerful ensemble learning method widely employed for both classification and regression tasks [33]. It leverages a collection of decision trees to formulate predictions. The underlying process entails the creation of bootstrap samples, which are randomly selected subsets drawn with replacement from the original dataset. Each decision tree processes its designated subset of data and produces its individual output. The ultimate prediction is derived by averaging the outcomes generated by all the decision trees. The Random Forest Regression algorithm unfolds as follows:

- Randomly choose some data points from the initial dataset.
- Determine the number of decision trees (N) to construct.
- Construct decision trees using subsets of the selected data points.
- Iteratively repeat steps 1 and 3 to create multiple decision trees.
- The final predicted output (Y) is calculated by averaging the individual outputs $(y_1, y_2, y_3 ... y_N)$ from all the decision trees.

Within the Random Forest algorithm, the dataset is partitioned into equal-sized subsets, with the possibility of some rows being duplicated across subsets, and each subset is assigned equal importance. The predictions are then generated based on the mean evaluation. This ensemble approach enhances the robustness and precision of predictions in various applications.

2.3.3 *Extreme Gradient Boosting Technique*

XGBoost (Extreme Gradient Boosting) is a powerful library for regression and classification tasks [34, 35]. Its key advantages are speed, scalability, and parallel computation. It converts weak learners into strong ones using boosting. In XGBoost, estimators (trees) are sequentially added to the ensemble model to improve the accuracy by adding a base learner to correct the shortcomings of the existing base models. In this study, ensemble-based algorithms including Random Forest and XGBoost were used because they are believed to improve accuracy by decreasing the variance in the prediction [34, 35].

$$\hat{y}_i = \sum_{k=1}^{K} f_k(x_i), \quad f_k \in \mathcal{F} \tag{5}$$

$$\mathcal{F} = \{f \mid f(x) = w_{q(x)}\} \tag{6}$$

where K is the number of regression trees, $\hat{y}_i$ is the predicted value for input x_i, x_i is the input value, $\mathcal{F}$

is the set of regression trees, f_k is the k-th decision tree, w is the weight vector of the regression tree, and q represents the structure of the tree.

The objective function can be stated as follows:

$$\mathcal{L} = \sum_{i=1}^{n} l(y_i, \hat{y}_i) + \sum_{k=1}^{K} \Omega(f_k) \tag{7}$$

where $l(y_i, \hat{y}_i)$ is the discrepancy between the real value y_i and the predicted value $\hat{y}_i$, and Ω is the regularization term, which is employed to prevent overfitting of the model.

2.3.4 Description of the Support Vector Machine Technique

SVM is an ML theory framework and a general method established on a set of finite samples [36]. Practical problems such as small samples, nonlinear analysis, and local minimum points can be solved by SVM. The basic concept is that through some preselected nonlinear reflection, input data are mapped into a high-dimensional space in which the optimal classification hyperplane is formed.

In terms of SVM function fitting problems, it is actually a problem to fit data $\{x_i, y_i\}, (i = 1, 2, 3, \ldots, n), x_i \in \mathbb{R}^d, y_i \in \mathbb{R}$ with function $f(x) = w \cdot x + b$. According to the SVM theory, the function of the fitting problem is given as

$$f(x) = w \cdot x + b = \sum_{i=1}^{n} (\alpha_i - \alpha_i^*) K(x, x_i) + b \tag{8}$$

where α_i, α_i^*, b are obtained by solving the subsequent optimization problems. Usually a small fraction of α_i, α_i^* are non-zero, which are called support vectors.

The radial basis kernel function hyperparameter which was used in the SVM model is given as

$$K(x, y) = \exp\left(-\frac{\|x - y\|^2}{\sigma^2}\right) \tag{9}$$

2.4 Performance Metrics

The accuracy of the prediction of the ML methods was measured using the coefficient of determination (R^2), Root Mean Squared Error ($RMSE$), and Bayesian Information Criterion (BIC) to understand the target against variations of individual independent variables. The R^2 is a statistical index with the model having an optimum value closer to 1, and the $RMSE$ gets closer to zero for an accurate model [37]. Equations (9), (10), and (11) illustrate the mathematical expressions used for R^2, $RMSE$, and BIC, respectively:

$$R^2 = \frac{\left[\sum_{i=1}^{n}(O_i - \bar{O})(P_i - \bar{P})\right]^2}{\sum_{i=1}^{n}(O_i - \bar{O})^2 \sum_{i=1}^{n}(P_i - \bar{P})^2} \tag{10}$$

$$RMSE = \sqrt{\frac{1}{n}\sum_{i=1}^{n}\left(EP_{\text{observed}} - EP_{\text{predicted}}\right)^2} \tag{11}$$

where n is the total number of cumulative enthalpy production data points observed, EP_{observed} is the enthalpy production observed data points, $\bar{O}$ is the mean of the observed data points, and $\bar{P}$ is the mean of the predicted data points.

$$BIC = -2\ln(L) + k\ln(n) \tag{12}$$

where L is the likelihood of the model given the data, k is the number of estimated parameters in the model, and n is the total number of data points used in the model fitting.

3 Results and Discussion

3.1 Numerical Model Description

The model included nine wells: seven production wells producing hot water/steam and two injection wells, which were used for the field-scale simulation of enthalpy production. The reservoir measured roughly 6400 m, 6400 m, and 140 m in the X, Y, and Z directions, respectively. A total of 96000 grid blocks were used corresponding to eighty grid blocks in both the X and Y directions and fifteen grid blocks in the Z direction. In this simulation, cartesian grids were used. This approach allowed a better representation of the geological features and description of the reservoir especially for heterogeneities. The target reservoir is located at a depth of 2000 m. The active fluid phase in the model was water. To improve heat production, hydro-fracturing is implemented to enhance permeability in this reservoir. The target reservoir is considered to be a fractured medium. The model is composed of the target reservoir, injection, and production wellbores. Figure 5 is used to show the fluid flow and heat transfer process in the entire well/reservoir system. The reservoir model made use of the full symmetry domain of the reservoir to fully understand its energy dynamics. To simulate fluid

flow and heat transfer in fractures and matrix pores, dual-permeability multiple-interacting models were employed, meaning each grid block was composed of a matrix part and a fracture, as shown ideally in Figure 5.

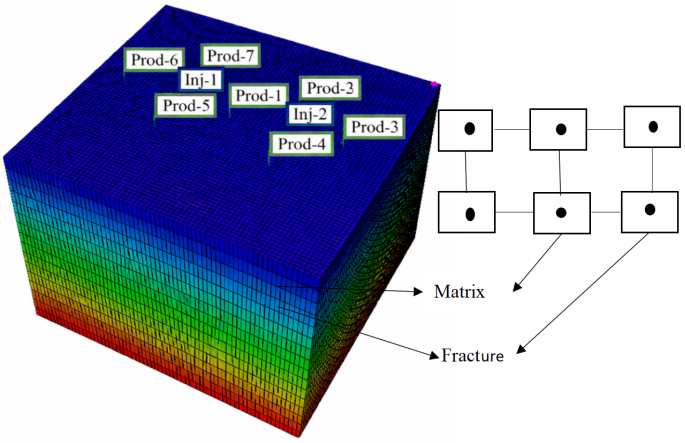

Figure 5. Geothermal reservoir model.

Well completion was implemented after the model was established. An inverted well pattern was adopted in the simulation, with both production and injection wells perforated across all fifteen grid layers of the model. The inverted well pattern refers to a configuration in which a single injection well is centrally located and surrounded by production wells. By placing the injection well at the center of each pattern, the injected fluid can spread outward symmetrically, thereby promoting more uniform heat sweep and improving the efficiency of the heat extraction process. All nine wells were designed as vertical wells.

3.2 Input and Target Dataset

A simulation study was carried out to obtain a simulation for input and output for training and testing to establish a mapping relationship. Table 4 shows the reservoir parameters used to run the simulation model and as the base case for the sensitivity analysis of various reservoir properties. The statistical summary of the dataset is presented in Table 5. The total dataset obtained from the RSM model experiment was 80 sample points, 70% of which was used for training and the rest 30% for testing the ML models.

The prediction of enthalpy production can be a function of multiple variables for the characteristics of the reservoir to be determined. The operational controllable input parameters for the RSM, Decision Tree, Random Forest, XGBoost, and Support Vector Machine models are Matrix Porosity, Matrix Permeability, Fracture Spacing, Permeability Anisotropy, Rock Heat Capacity, Rock Thermal Conductivity, and the target is the Cumulative Enthalpy Production as shown in Table 5.

3.3 Analysis of Reservoir Simulation Results

The base values used in the study are based on the reference of a dual-permeability reservoir. The pressure distributions of the fracture domain over the simulation periods are illustrated in Figure 6(a-d). Since the permeability in the fracture zone of the reservoir is significantly higher than that of the rock matrix, the advance of the cold front from the injection wells through the fracture network gradually extracts heat from the surrounding rock matrix before eventually reaching the production wells.

This process is governed by the interplay between advection and diffusion, which are the primary mechanisms controlling heat transfer in fractured media. Fracture spacing plays a critical role in this balance by influencing the rate and efficiency of heat exchange between the high-permeability fractures and the lower-permeability rock matrix. When fracture spacing is small, heat transfer is dominated by conduction (diffusion) due to the proximity of high-temperature matrix blocks to the flowing cold fluid in fractures. This enhances thermal recharge to the fluid, prolonging heat extraction and delaying premature thermal breakthrough at production wells. In contrast, when fracture spacing is large, advection becomes the dominant mechanism. The cold front advances rapidly through the fractures due to the high permeability, but heat conduction from the rock matrix is slower, resulting in a less effective energy exchange. This can lead to an incomplete thermal sweep, where a significant portion of the matrix remains underutilized, ultimately reducing the reservoir's overall thermal efficiency.

Furthermore, the hydraulic head difference between the fracture and matrix domains also impacts heat transfer efficiency. A higher-pressure gradient can drive faster fluid movement through the fractures, increasing the advective transport of cold water. This accelerates the thermal depletion of the reservoir, especially in cases where diffusion-driven heat transfer from the matrix is insufficient to replenish the thermal energy of the flowing fluid. The interaction between these transport mechanisms must be carefully considered to optimize geothermal reservoir performance.

Table 4. Reservoir parameters for the base model.

Parameters		Unit	Values
Reservoir	Thickness	m	136
	Reference Pressure	kPa	25
	Reference Depth	m	2000
	Reservoir Temperature	°C	170
	Fracture spacing	m	10
	Porosity		Matrix: 0.2
	Permeability	mD	Matrix: 25 Anisotropy: 0.1
	Rock grain density	kg/m^3	2440
	Rock thermal conductivity	$J/m^3day^\circ C$	2.1
	Rock specific heat capacity	$J/m^{3\circ}C$	2.347×10^6
Injection/Production strategy	Water Injection rate	m^3/day	8000
	Injector Bottomhole Pressure	kPa	35000
	Duration of heat extraction		20 years

Table 5. Statistical summary of dataset for cumulative enthalpy production prediction.

Variable	Unit	Minimum	Average	Maximum	Standard Deviation	Data Type
Matrix Porosity		0.15	0.2	0.25	0.03	Input
Matrix Permeability	mD	10	62	100	30.19	Input
Fracture Spacing	m	2	26	50	15.37	Input
Permeability Anisotropy		0.05	0.15	0.25	0.06	Input
Rock Heat Capacity (10^6)	$J/m^{3\circ}C$	1.76	2.35	2.93	0.38	Input
Rock Thermal Conductivity (10^3)	$J/m^3day^\circ C$	113	149	188	24.5	Input
Enthalpy Prod. Cum. (10^{16})	J	1.53	2.74	4.508	1.02	Output

Figure 7(a, b) illustrates the numerical simulation results for the base case, highlighting the interactions between key reservoir parameters. These findings suggest that further analysis of enthalpy production through controlled property variation is necessary. The proposed approach involves combining experimental design with machine learning and statistical analysis to systematically explore the impact of fracture geometry and thermal-hydraulic conditions on reservoir performance.

3.4 Enthalpy Production RSM-CCD Experimental Design

RSM modelling was implemented based on the CCD experimental design. In this study, a CCD was adopted that involves six independent variables: A (matrix porosity), B (matrix permeability), C (fracture spacing), D (permeability anisotropy), E (rock heat capacity), and F (rock thermal conductivity). The ranges for these variables, as presented in Table 6, are determined based on comprehensive

Table 6. Enthalpy production CCD, RSM experimental design space.

Experimental Variables	Unit	Levels		
		High-Level (+1)	Mid-Level (0)	Lower Level (-1)
A Matrix porosity		0.25	0.2	0.15
B Matrix Permeability (md)	mD	100	25	10
C Fracture spacing (m)	m	50	10	2
D Permeability Anisotropy		0.25	0.1	0.05
E Rock Heat Capacity	$J/m^{3o}C$	2.94E6	2.3E6	1.76E6
F Rock Thermal Conductivity	$J/mday^oC$	1.87E5	1.5E5	1.13E5

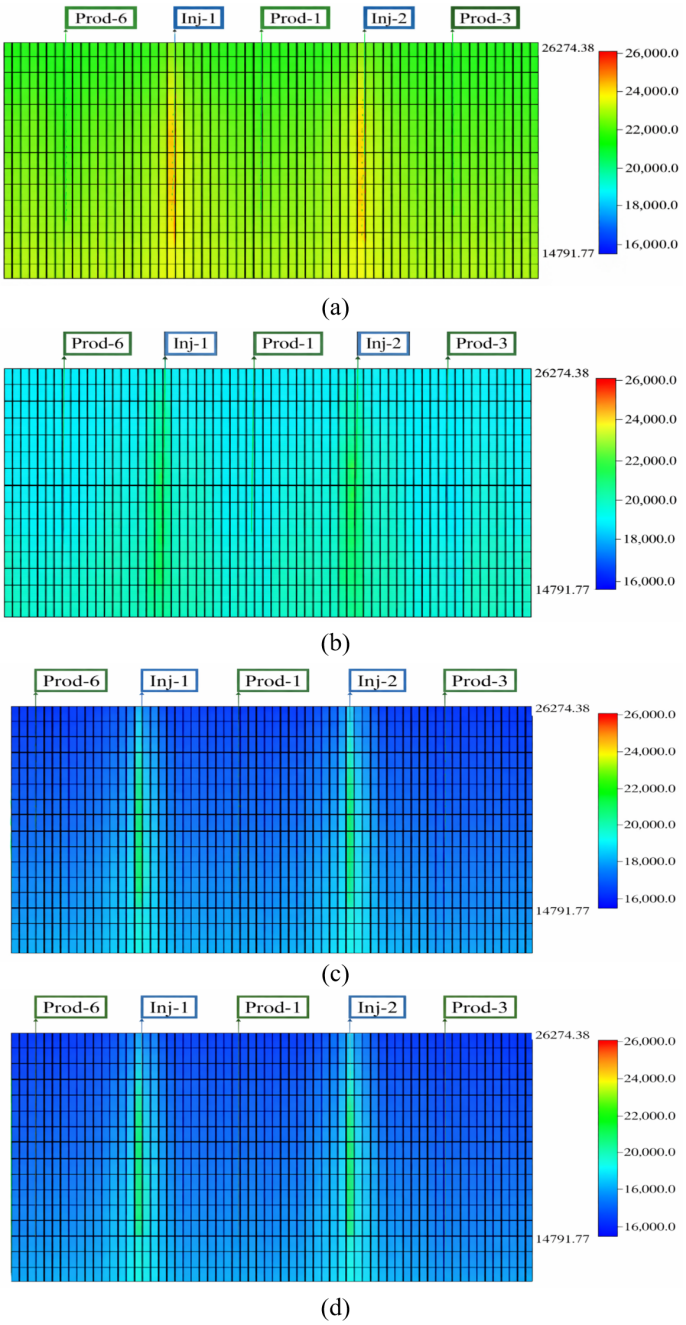

Figure 6. Pressure distributions for the fracture domain for the simulation period (a) 5 years (b) 10 years (c) 15 years (d) 20 years.

reviews of existing literature and analysis of field data from comparable geothermal systems. This approach ensures that the model encapsulates realistic operational scenarios. For instance, porosity values in geothermal reservoirs typically range from 0.2% to over 25%, depending on the rock type and geological setting [38].

Similarly, permeability and thermal conductivity values are selected to reflect conditions observed in actual geothermal reservoirs, thereby enhancing

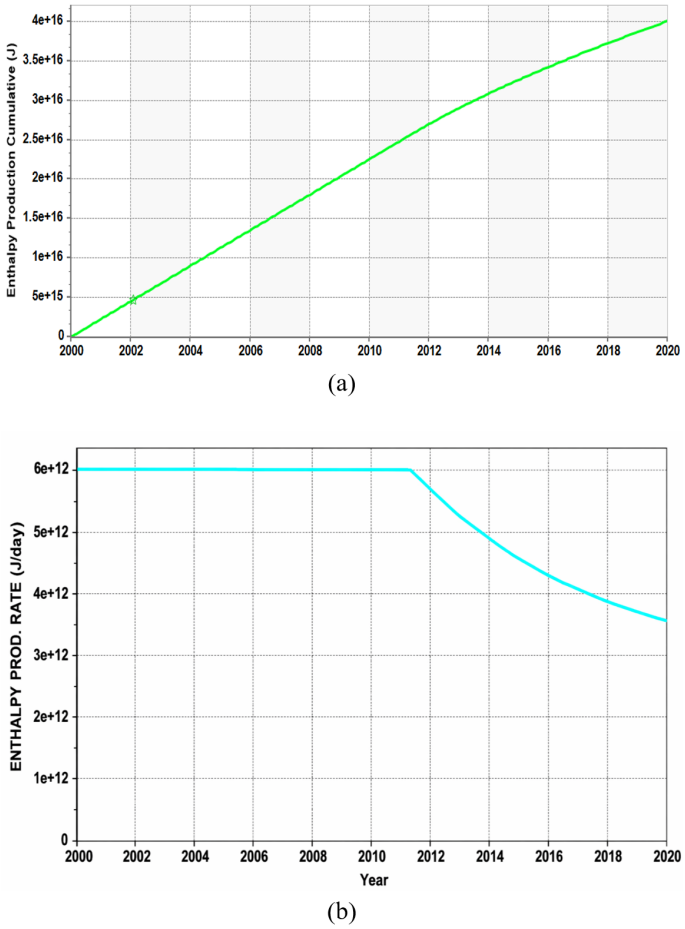

Figure 7. Simulation results (a) cumulative enthalpy production (entire field) (b) enthalpy production rate.

the model's validity and applicability. The targeted response (dependent variable) in this study is the cumulative enthalpy produced.

3.5 Development and Evaluation of RSM Enthalpy Production Models

3.5.1 Enthalpy Production RSM Model Development

Table 7 presents the experimental variables for the model development. CMG CMOST-aided regression analyses were used to fit the data in Table 5 into Equation (1) for the development of the RSM model. The second-order polynomial equation generated from the fitting as displayed in equation (13) shows all the single terms A, B and C (the single effects), AC and BC (2- way interaction effects), squared terms B2 and C2 model terms. The selection of second-order (quadratic) polynomials in RSM was a deliberate choice grounded in their ability to model curvature in the response surface effectively. Moreover, second-order polynomial models are relatively straightforward to estimate and apply, even when the underlying process is not fully understood.

Some terms generated were insignificant in the cumulative enthalpy production model, but when they interacted with other terms, they generated higher terms that became significant. The lower terms were left in the model to satisfy hierarchical effects as required by RSM.

The final empirical model for enthalpy production is expressed as a second-order polynomial in terms of the actual parameters A, B, and C:

$$\begin{aligned}\text{Enthalpy Production} = {} & 4.68412 \times 10^{16} \\ & - 1.13804 \times 10^{15}\, C \\ & + 1.91713 \times 10^{13}\, B \\ & + 2.30169 \times 10^{14}\, A \\ & + 8.65207 \times 10^{12}\, C^2 \\ & + 1.54477 \times 10^{11}\, BC \\ & + 4.56709 \times 10^{14}\, AC \\ & + 1.73648 \times 10^{11}\, B^2\end{aligned} \tag{13}$$

where A, B, and C are the actual input parameters.

3.5.2 *Effects Estimates for Quadratic RSM*

The main effects and the evaluation of proportional contributions of the two-way interaction (hierarchical influence) on the cumulative enthalpy produced in the form of charts are represented in Figure 8(a, b). Consequently, the height of the graph proportionally indicates the relative importance of the parameters on the EP responses; the high bar reflects a greater significant influence and the low bar reflects otherwise. Consequently, factor C mainly controlled the cumulative enthalpy produced, while interactions between AC were the most important combined effect factors. Matrix porosity was the third most important factor, as indicated in Figure 8.

The effects estimates results, shown in Figure 8(b), illustrate the effect estimates of various parameters on cumulative enthalpy production ("Enthalpy Prod Cum (J)").

Nat_Frac_Spacing represents Fracture Spacing, Por_Matrix represents Matrix Porosity, and PermH_Matrix denotes Permeability Anisotropy. The parameters "Minimum" and "Maximum" represent the least and highest enthalpy produced, which are 1.53×10^{16} and 4.507×10^{16}, respectively. "Nat_Frac_Spacing (2, 50)" exhibits a strong negative effect, indicating that wider fracture spacing reduces

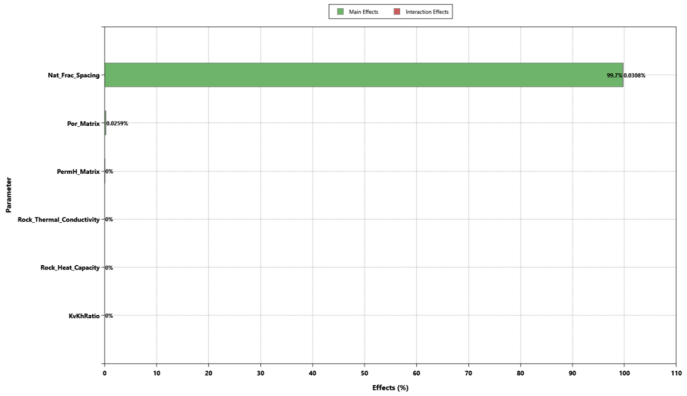

(a)

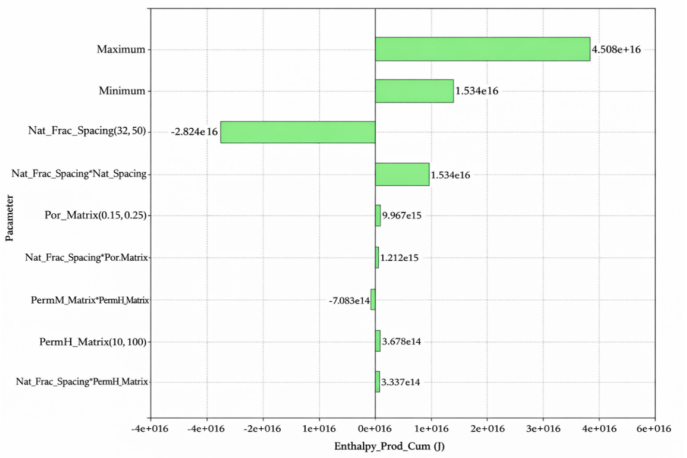

(b)

Figure 8. a. Diagram of the standardized effects for RSM b. Diagram of the two-way interaction effects for RSM.

enthalpy production, while "Nat_Frac_Spacing × Nat_Frac_Spacing" shows a positive effect of 9.851×10^{15}, highlighting a nonlinear relationship. Moderate effects are observed for parameters such as "Por_Matrix (0.15, 0.25)" (1.281×10^{15}), with smaller contributions from interactions like "PermH_Matrix × Rock_Thermal_Conductivity". This analysis identifies key parameters and interactions, such as "Nat_Frac_Spacing" and "Nat_Frac_Spacing × Por_Matrix," as critical to optimizing cumulative enthalpy production.

3.5.3 *Validation of Enthalpy Production Prediction RSM*

To produce a good model and well-fitted to the response surface parameter, three main indicators should be considered, which are the R square value (R-sq), the adjusted R square value (R-sq) and RMSE which can be found in variance (ANOVA) analysis. The coefficient of determination (R^2) of the developed model is 0.9994, indicating that the fitted regression model is capable of modelling 99.94% of the overall dataset. The adjusted R^2 of the model is 0.9993. This

Table 7. Experimental variables and results for cumulative enthalpy production (J).

Permeability Anisotropy	Fracture Spacing	Matrix Permeability	Matrix Porosity	Rock Heat Capacity (10^6)	Rock Thermal Conductivity (10^5)	Enthalpy Produced (10^{16})
0.1	10	25	0.2	2.35	1.50	4.004935
0.05	2	10	0.15	1.76025	1.125	4.498965
0.05	2	10	0.15	1.76025	1.875	4.499349
0.05	2	10	0.15	2.93375	1.125	4.507415
0.05	2	10	0.15	2.93375	1.875	4.50752
0.05	2	10	0.25	1.76025	1.125	4.500434
0.05	2	10	0.25	1.76025	1.875	4.500661
0.05	2	10	0.25	2.93375	1.125	4.50607
0.05	2	10	0.25	2.93375	1.875	4.506172
0.05	2	100	0.15	1.76025	1.125	4.498572
0.05	2	100	0.15	1.76025	1.875	4.498902
0.05	2	100	0.15	2.93375	1.125	4.507456
0.05	2	100	0.15	2.93375	1.875	4.507534
0.05	2	100	0.25	1.76025	1.125	4.500476
0.05	2	100	0.25	1.76025	1.875	4.500633
0.05	2	100	0.25	2.93375	1.125	4.50623
0.05	2	100	0.25	2.93375	1.875	4.506305
0.05	26	55	0.2	2.347	1.5	2.63508
0.05	50	10	0.15	1.76025	1.125	1.529821
0.05	50	10	0.15	1.76025	1.875	1.53234
0.05	50	10	0.15	2.93375	1.125	1.544752
0.05	50	10	0.15	2.93375	1.875	1.547767
0.05	50	10	0.25	1.76025	1.125	1.740552
0.05	50	10	0.25	1.76025	1.875	1.741904
0.05	50	10	0.25	2.93375	1.125	1.755132
0.05	50	10	0.25	2.93375	1.875	1.756636
0.05	50	100	0.15	1.76025	1.125	1.587905
0.05	50	100	0.15	1.76025	1.875	1.590614
0.05	50	100	0.15	2.93375	1.125	1.603187
0.05	50	100	0.15	2.93375	1.875	1.606448
0.05	50	100	0.25	1.76025	1.125	1.816828
0.05	50	100	0.25	1.76025	1.875	1.818269
0.05	50	100	0.25	2.93375	1.125	1.832264
0.05	50	100	0.25	2.93375	1.875	1.833873
0.15	2	55	0.2	2.347	1.5	4.504604
0.15	26	10	0.2	2.347	1.5	2.508409
0.15	26	55	0.15	2.347	1.5	2.365621
0.15	26	55	0.2	1.76025	1.5	2.618475
0.15	26	55	0.2	2.347	1.125	2.635069
0.15	26	55	0.2	2.347	1.5	2.636575
0.15	26	55	0.2	2.347	1.875	2.637847
0.15	26	55	0.2	2.93375	1.5	2.651109
0.15	26	55	0.25	2.347	1.5	2.848068
0.15	26	100	0.2	2.347	1.5	2.654923
0.15	50	55	0.2	2.347	1.5	1.725774
0.25	2	10	0.15	1.76025	1.125	4.49898
0.25	2	10	0.15	1.76025	1.875	4.499364
0.25	2	10	0.15	2.93375	1.125	4.507418
0.25	2	10	0.15	2.93375	1.875	4.507523
0.25	2	10	0.25	1.76025	1.125	4.500441
0.25	2	10	0.25	1.76025	1.875	4.500668
0.25	2	10	0.25	2.93375	1.125	4.506071
0.25	2	10	0.25	2.93375	1.875	4.506173
0.25	2	100	0.15	1.76025	1.125	4.498761
0.25	2	100	0.15	1.76025	1.875	4.499107
0.25	2	100	0.15	2.93375	1.125	4.507494
0.25	2	100	0.15	2.93375	1.875	4.507576
0.25	2	100	0.25	1.76025	1.125	4.500549
0.25	2	100	0.25	1.76025	1.875	4.500732
0.25	2	100	0.25	2.93375	1.125	4.506258
0.25	2	100	0.25	2.93375	1.875	4.506335
0.25	26	55	0.2	2.347	1.5	2.63751
0.25	50	10	0.15	1.76025	1.125	1.531805
0.25	50	10	0.15	1.76025	1.875	1.534228
0.25	50	10	0.15	2.93375	1.125	1.546669
0.25	50	10	0.15	2.93375	1.875	1.54959
0.25	50	10	0.25	1.76025	1.125	1.743134
0.25	50	10	0.25	1.76025	1.875	1.744452
0.25	50	10	0.25	2.93375	1.125	1.757706
0.25	50	10	0.25	2.93375	1.875	1.759176
0.25	50	100	0.15	1.76025	1.125	1.588355
0.25	50	100	0.15	1.76025	1.875	1.590815
0.25	50	100	0.15	2.93375	1.125	1.603586
0.25	50	100	0.15	2.93375	1.875	1.606606
0.25	50	100	0.25	1.76025	1.125	1.817662
0.25	50	100	0.25	1.76025	1.875	1.819017
0.25	50	100	0.25	2.93375	1.125	1.833077
0.25	50	100	0.25	2.93375	1.875	1.834603

Table 8. Analysis of variance for quadratic RSM.

Source	Degrees of Freedom	Sum of Squares	Mean Square	F Ratio	Prob F
Model	7	1.34138×10^{34}	1.91626×10^{33}	16539.7	0.00001
Error	69	7.99421×10^{30}	1.15858×10^{29}	-	-
Total	76	1.34218×10^{34}	-	-	-

value is represented by how much the model explains the variation in the response used. Also, Figure 9(a) shows the RSM model predicted value as against the actual values. Based on this result, it was shown that the model explains a very high percentage of the total variation in the response.

The model accounts for nearly all the variability in the dataset, as evidenced by the model Sum of Squares (1.34138×10^{34}) in Table 8, which represents an overwhelming proportion of the Total Sum of Squares (1.34218×10^{34}). The remaining variability, represented by the error Sum of Squares (7.99421×10^{30}), is minimal, indicating that the residuals are relatively small. With a high F-ratio of 16,539.7 and an exceptionally low p-value (< 0.00001), the likelihood of the observed results occurring by random chance is negligible, confirming the statistical significance of the model. Furthermore, the model Mean Square (1.91626×10^{33}) is vastly larger than the Error Mean Square (1.15858×10^{29}), further supporting the model's effectiveness in capturing the relationship between the variables.

The plot in Figure 9(b) presents the distribution and cumulative probability of cumulative enthalpy production values. The green histogram represents the frequency distribution, where the y-axis on the left denotes the relative frequency as a percentage, and the x-axis shows the cumulative enthalpy production values in Joules. The blue line overlays the cumulative probability curve, with the y-axis on the right representing the cumulative probability as a fraction (0 to 1).

The histogram indicates that a substantial portion of the observations is concentrated at the extremes of the distribution. The first bar (1.5×10^{16} to 2.0×10^{16} Joules) accounts for 36.2% of the total observations, indicating a significant clustering of data in the lower range of enthalpy production. Conversely, the final bar (4.5×10^{16} to 5.0×10^{16}) contains the largest proportion of observations at 41.2%, revealing a second concentration at the higher end. The mid-range values exhibit much lower frequencies, with only 6.2%, 1.2%, and 2.5% of observations in the 2.0×10^{16} to 3.5×10^{16} Joules range. This bimodal distribution

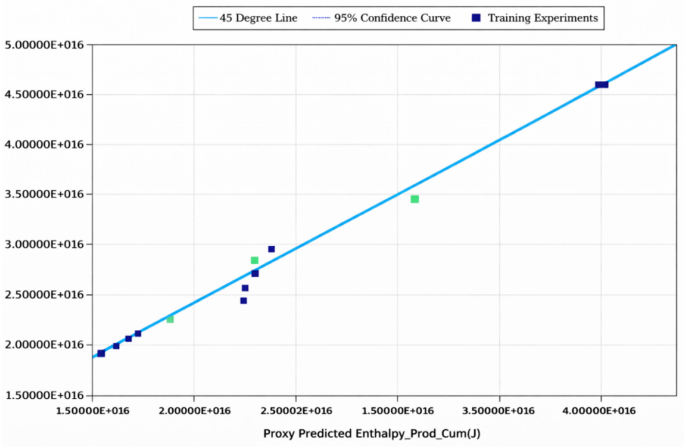

(a)

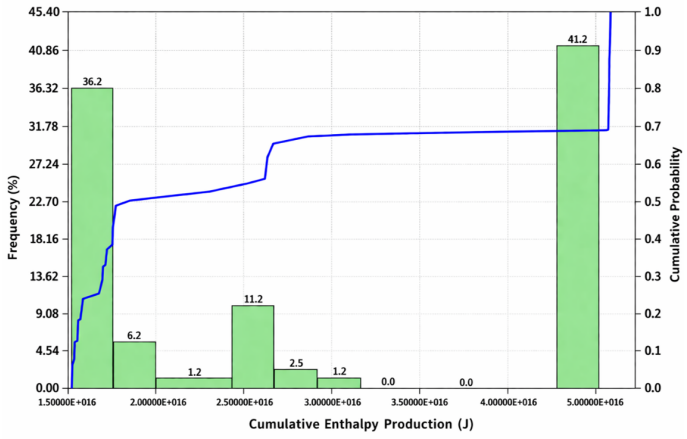

(b)

Figure 9. Plots for the RSM model (a) simulated vs proxy models (b) Normal probability and histogram.

suggests distinct operational conditions or factors driving enthalpy production at these extremes.

The cumulative probability curve provides a complementary perspective, illustrating the cumulative proportion of observations as enthalpy production values increase. The steep rise at the lower range corresponds to the high concentration of data in the first histogram bar. The curve then progresses more gradually across the mid-range values due to the lower frequency in this region. Toward the higher range, the curve rises sharply again, reflecting the substantial concentration of observations in the final bar.

The bimodal nature of the distribution highlights the presence of two dominant operational states or conditions influencing enthalpy production. The high concentration at the lower range may represent baseline or standard operational scenarios with lower energy demands or simpler production processes. In contrast, the spike at the higher range could indicate conditions associated with peak performance, high demand, or more complex production scenarios.

3.5.4 Influence of the Operational Parameter of Enthalpy Production and Optimization

In this study, the PSO model was applied to the RSM dataset framework. The RSM approach was employed as a basis to design and create a dataset comprising 500 experimental data points as shown in Figure 10(a). These data points represent various parameter configurations and their corresponding outcomes, which serve as the input space for the optimization process.

The PSO model systematically explored this dataset through iterative means to identify the parameter combinations that yield the optimized cumulative enthalpy production. By leveraging the efficiency of PSO, the model was able to converge towards optimal solutions while maintaining computational efficiency. The results include the general solution, base case, and optimal solution data points, as illustrated in the plot in Figure 10(a).

The identified optimal operating parameters include matrix porosity = 0.15, matrix permeability = 100 mD, permeability anisotropy = 0.25, fracture spacing = 2 m, rock heat capacity = 2.93×10^6 J/m^3 °C, rock thermal conductivity = 1.88×10^5 J/m·day °C, and cumulative enthalpy produced = 4.507×10^{16} J as the best conditions. The optimal cumulative enthalpy production is further illustrated in the histogram presented in Figure 10(b), where the majority of the enthalpy production is concentrated around a value of 4.5075×10^{16} J.

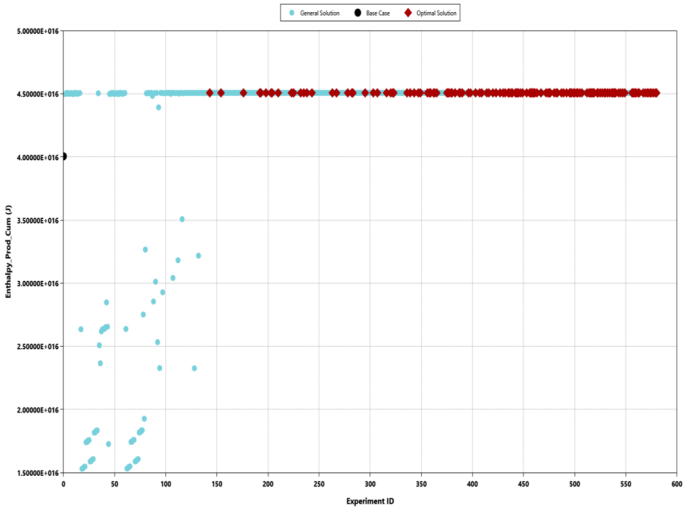

(a)

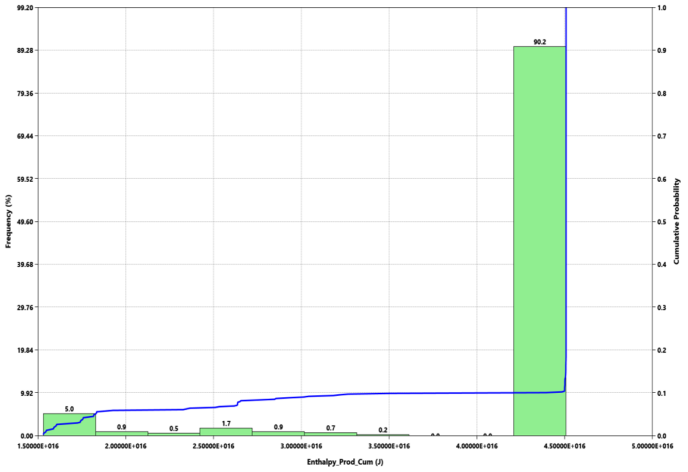

(b)

Figure 10. Plots for the PSO model (a) optimization solution (b) normal probability and histogram.

3.6 Random Forest, Decision Tree, XGBoost, and Support Vector Machine Prediction of Data for Cumulative Enthalpy Production

3.6.1 Correlational Analysis of the Effect of Independent Features

The correlation heatmap for the input parameters and the response is shown in Figure 11 from the exploratory data analysis. The feature fracture spacing exhibits a strong negative correlation with the target response. This implies that any small changes in this feature will have a direct impact on the target response. The other features do not show a strong positive or negative correlation with the target response. Consequently, variations in these independent columns may not result in significant variations in the target response. Overall, the analysis suggests that the fracture spacing feature is highly influential in predicting the target response, while the matrix spacing, matrix permeability, permeability anisotropy, rock heat capacity, and rock thermal conductivity features have a relatively lesser impact. This finding is also substantiated by the effects estimate plot of the RSM model in Figure 8(a).

3.6.2 ML Techniques Modeling

For comparisons, Decision Tree, Random Forest, XGBoost, and Support Vector Machine models are trained on RSM data to predict enthalpy production in the geothermal reservoir. It is obvious from the

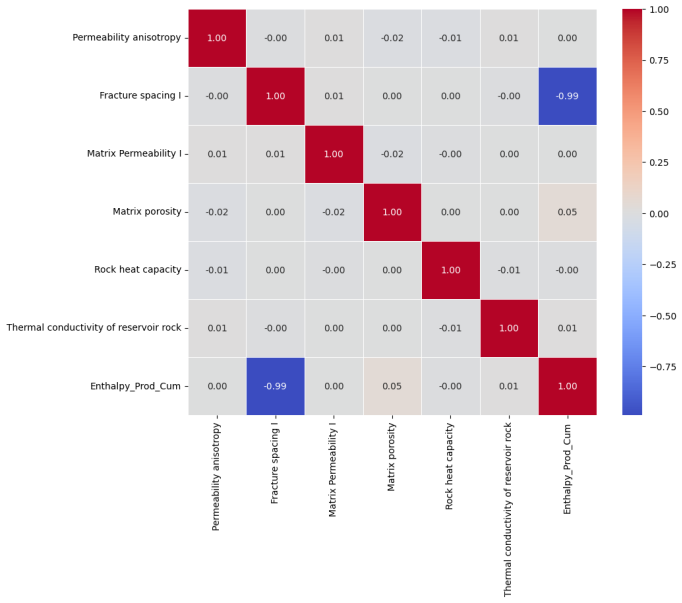

Figure 11. Heatmap representing the correlation.

results that the fittings for the ML models of the data were lower compared with the RSM prediction. This is manifested in the Y = X line (Figure 12) showing the prediction potentials of the four models, indicating better performance for the Random Forest model, although the others are not far off. Figure 12 (a-d) shows the plot for observed and predicted enthalpy production for the models used in this study. The proximity between observed and predicted data points suggests the robustness of the ML models in predicting enthalpy production.

In this analysis, the evaluation of the performance of the models using predicted versus residual plots is illustrated in Figure 13(a-d). These plots reveal important insights into the behavior and precision of the regression models under scrutiny. It is crucial to note that the residuals consistently sum up to zero in all regression models, a phenomenon visually represented by the dark zero line in Figure 13(a-d). An effective residual plot is characterized by the majority of data points closely aligned with the zero line, signaling a minimal deviation from the expected values.

Zooming in on Figure 13(a), the residuals for the Random Forest model are confined within the range of ± 0.2, reflecting strong predictive accuracy. The Decision Tree model, as shown in Figure 13(b), demonstrates a slightly broader range, with residuals contained within ± 0.4, apart from a single outlier. This suggests that while the Decision Tree performs well overall, it may occasionally struggle with extreme cases. The XGBoost model, depicted in Figure 13(c), exhibits strong predictive reliability, with residuals

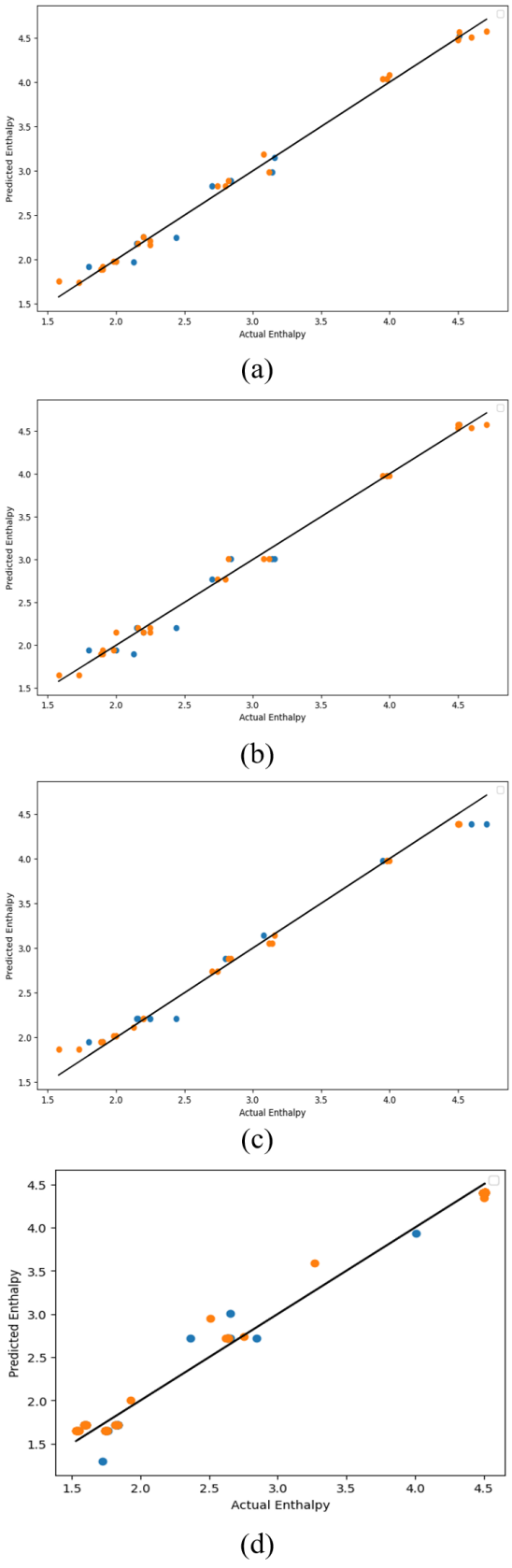

Figure 12. ML training and testing models predicted vs. experimental plots (a) Random Forest (b) Decision Tree (c) XGBoost (d) Support Vector Machine.

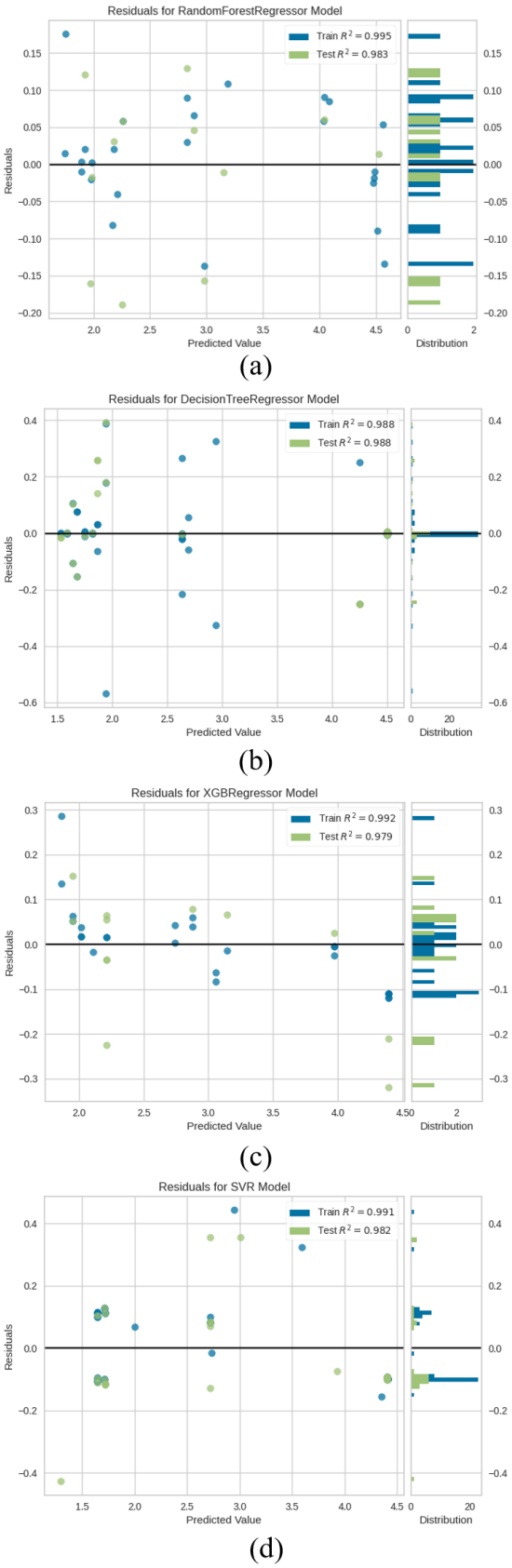

Figure 13. ML training and testing models' residual plots (a) Random Forest (b) Decision Tree (c) XGBoost (d) Support Vector Machine.

predominantly within ± 0.3 and an outlier, indicating its robustness across varied scenarios. In contrast, the SVM model, illustrated in Figure 13(d), shows residuals largely within ± 0.4 but with two notable outliers. This pattern may suggest a tendency for overprediction in certain instances, emphasizing the need for further fine-tuning or regularization to enhance its performance.

Noteworthy is the observation that the magnitudes of negative residuals are nearly equivalent to their positive counterparts. This symmetry suggests the model does not exhibit a strong bias toward overprediction or underprediction, which is indicative of balanced performance. However, the presence of outliers may indicate sensitivity to specific features in the dataset.

3.7 Machine Learning Techniques and RSM Comparative Performance

The predictive fitting parameters developed for the Random Forest, Decision Tree, XGBoost, Support Vector Machine, and RSM models for cumulative enthalpy production (EP) are presented in Table 9. Evaluation metrics, such as the R^2 score and $RMSE$, were used to assess the predictive performance of each model. The R^2 score measures the proportion of variance in the dependent variable explained by the model, whereas $RMSE$ quantifies the average magnitude of the errors in the predictions. These metrics provide key insights into the strengths and weaknesses of each modeling approach. The R^2 score for the RSM model was 0.999404, slightly outperforming the Random Forest (0.9929), Decision Tree (0.9882), XGBoost (0.9883), and Support Vector Machine (0.9888) models. This suggests that the RSM model accounts for a marginally larger proportion of variance in cumulative enthalpy production than the machine learning models. Similarly, the relatively low $RMSE$ values for the RSM (0.034) and Random Forest (0.103) models indicate superior predictive accuracy compared to the Decision Tree (0.1360), XGBoost (0.142), and Support Vector Machine (0.1629) models. However, it is important to note that the RSM model's higher performance may be partly attributed to its reliance on data without splitting into training and testing sets, unlike the machine learning models, which were trained on 70% of the data and tested on the remaining 30%. This methodological distinction suggests that while the RSM model demonstrates high accuracy within the confines of the available data, its performance may not generalize as effectively

to new datasets. Additionally, the RSM model was specifically designed based on data from the CCD study, inherently optimizing its performance for this dataset. The BIC values suggest that the Random Forest model (-84.9822) offers a better balance of fit and complexity compared to the Decision Tree (-9.5023), XGBoost (-59.8092), and Support Vector Machine (-14.0142) models. This highlights the Random Forest's efficiency in leveraging its complexity to achieve accurate predictions without overfitting.

Table 9. ML techniques and RSM fitted model parameters for cumulative enthalpy produced.

Model	Parameter	EP
RSM	R^2	0.999404
	$RMSE$	0.034
Random Forest Regression	Training R^2	0.9953
	Testing R^2	0.9830
	Overall R^2	0.9929
	$RMSE$	0.103
	BIC	-84.9822
Decision Tree Regressor	Training R^2	0.9882
	Testing R^2	0.9881
	Overall R^2	0.9882
	$RMSE$	0.1360
	BIC	-9.5023
XGBoost	Training R^2	0.9985
	Testing R^2	0.9790
	Overall R^2	0.9883
	$RMSE$	0.142
	BIC	-59.8092
Support Vector Machine	Training R^2	0.9914
	Testing R^2	0.9816
	Overall R^2	0.9888
	$RMSE$	0.1629
	BIC	-14.0142

Complex models such as Random Forests and XGBoost can capture intricate patterns within the data as shown by the BIC value but are susceptible to overfitting, especially with limited or unrepresentative training data. Simpler models like Decision Trees may not capture all data complexities, leading to underfitting. Balancing model complexity is essential for optimal predictive performance. For future modeling efforts, implementing consistent data partitioning strategies, such as k-fold cross-validation, is recommended to ensure fair performance comparisons. Careful feature selection and engineering can improve model performance by reducing complexity and the risk of overfitting. Applying regularization methods like Lasso or Ridge regression can constrain model parameters, promoting simpler models that generalize better to unseen data. Recent advances have also demonstrated novel machine learning approaches for reservoir temperature prediction, further highlighting the growing capability of data-driven methods in geothermal applications [44].

4 Conclusions

In this study, the cumulative enthalpy production of an enhanced geothermal system was modeled using RSM, Random Forest, Decision Tree, XGBoost, and Support Vector Machine, and their predictive performances were compared based on R^2 and $RMSE$. The RSM model achieved the highest R^2 of 0.999404, outperforming all ML models evaluated. Residual plots of the parameters and responses were used to determine the presence or absence of any general trend of association. The effects estimate plots and the Analysis of Variance (ANOVA) were generated between the various input parameters to reveal the parameter with the most influence on the enthalpy. The PSO numerical solutions of optimal operating conditions for the best cumulative enthalpy produced were also studied from the RSM model. On the basis of the results obtained, the following conclusions were reached:

1. The PSO study identified optimal operating parameters for the geothermal system, which include a matrix porosity of 0.15, matrix permeability of 100 mD, permeability anisotropy of 0.25, fracture spacing of 2 m, rock heat capacity of 2.93×10^6 J/m^3 °C, and rock thermal conductivity of 1.88×10^5 J/m·day °C. These parameters yielded a cumulative enthalpy production of 4.507×10^{16} J, demonstrating their effectiveness in enhancing geothermal energy extraction.

2. While the ML models, including Random Forest, Decision Tree, XGBoost, and Support Vector Machine, achieved acceptable performance, their generalizability may be limited by the relatively small dataset (80 sample points) obtained from the RSM-based experimental design, as well as the 70/30 training-testing data partition employed in this study.

3. Increasing the data volume through additional RSM simulations, combined with a focus on multiple response parameters, could further refine our understanding of observed patterns and improve the depth of predictive analysis. This approach may lead to more accurate and generalized models.

4. A promising avenue for future research involves evaluating the performance of Deep Learning models in enthalpy prediction when integrated with metaheuristic algorithms such as genetic algorithms. These techniques could be used to optimize hyperparameters, potentially enhancing the predictive accuracy and robustness of the ML models.

Data Availability Statement

Data will be made available on request.

Funding

This work was supported without any funding.

Conflicts of Interest

The authors declare no conflicts of interest.

AI Use Statement

The authors declare that no generative AI was used in the preparation of this manuscript.

Ethical Approval and Consent to Participate

Not applicable.

References

[1] He, J., Li, K., Wang, X., Gao, N., Mao, X., & Jia, L. (2022). A Machine Learning Methodology for Predicting Geothermal Heat Flow in the Bohai Bay Basin, China. *Natural Resources Research, 31*(1), 237-260. [CrossRef]

[2] Hou, J., Cao, M., & Liu, P. (2018). Development and Utilization of Geothermal Energy in China: Current Practices and Future Strategies. *Renewable Energy, 125*, 401-412. [CrossRef]

[3] Li, K., Bian, H., Liu, C., Zhang, D., & Yang, Y. (2015). Comparison of Geothermal with Solar and Wind Power Generation Systems. *Renewable & Sustainable Energy Reviews, 42*, 1464-1474. [CrossRef]

[4] Zhang, C., Wang, X., Jiang, C., & Zhang, H. (2023). Numerical simulation of geothermal energy production from hot dry rocks under the interplay between the heterogeneous fracture and stimulated reservoir volume. *Journal of Cleaner Production, 414*, 137724. [CrossRef]

[5] Suzuki, A., Fomin, S. A., Chugunov, V. A., Niibori, Y., & Hashida, T. (2016). Fractional Diffusion Modeling of Heat Transfer in Porous and Fractured Media. *International Journal of Heat and Mass Transfer, 103*, 611-618. [CrossRef]

[6] Zeng, Y. C., Su, Z., & Wu, N. Y. (2013). Numerical simulation of heat production potential from hot dry rock by water circulating through two horizontal wells at Desert Peak geothermal field. *Energy, 56*, 92-107. [CrossRef]

[7] Zhang, C., Jiang, G., Jia, X., Li, S., Zhang, S., Hu, D., ... & Wang, Y. (2019). Parametric study of the production performance of an enhanced geothermal system: A case study at the Qiabuqia geothermal area, northeast Tibetan plateau. *Renewable energy, 132*, 959-978. [CrossRef]

[8] Wang, S., Huang, Z., Wu, Y. S., Winterfeld, P. H., & Zerpa, L. E. (2016). A semi-analytical correlation of thermal-hydraulic-mechanical behavior of fractures and its application to modeling reservoir scale cold water injection problems in enhanced geothermal reservoirs. *Geothermics, 64*, 81-95. [CrossRef]

[9] Gudala, M., & Govindarajan, S. K. (2021). Numerical investigations on a geothermal reservoir using fully coupled thermo-hydro-geomechanics with integrated RSM-machine learning and ARIMA models. *Geothermics, 96*, 102174. [CrossRef]

[10] Jiang, A., Qin, Z., Faulder, D., Cladouhos, T. T., & Jafarpour, B. (2022). Recurrent Neural Networks for Short-term and Long-term Prediction of Geothermal Reservoirs. *Geothermics, 104*, 102439. [CrossRef]

[11] Assouline, D., Mohajeri, N., Gudmundsson, A., & Scartezzini, J. L. (2019). A machine learning approach for mapping the very shallow theoretical geothermal potential. *Geothermal Energy, 7*(1), 19. [CrossRef]

[12] Rezvanbehbahani, S., Stearns, L. A., Kadivar, A., Walker, J. D., & van der Veen, C. J. (2017). Predicting the geothermal heat flux in Greenland: A machine learning approach. *Geophysical Research Letters, 44*(24), 12-271. [CrossRef]

[13] Spichak, V., Geiermann, J., Zakharova, O., Calcagno, P., Genter, A., & Schill, E. (2015). Estimating deep temperatures in the Soultz-sous-Forêts geothermal area (France) from magnetotelluric data. *Near Surface Geophysics, 13*(4), 397-408. [CrossRef]

[14] Ishitsuka, K., Kobayashi, Y., Watanabe, N., Yamaya, Y., Bjarkason, E. K., Suzuki, A., Mogi, T., Asanuma, H., Kajiwara, T., Sugimoto, T., & Saito, R. (2021). Bayesian and Neural Network Approaches to Estimate Deep Temperature Distribution for Assessing a Supercritical Geothermal System: Evaluation Using a Numerical Model. *Natural Resources Research, 30*(5), 3289-3314. [CrossRef]

[15] Maharsi, D. A., Ta'dung, J. C., Jannoke, L., & Budi, I. S. (2022). Sensitivity Analysis Using One-Factor-at-a-Time and Response Surface Method in Liquid-Dominated Geothermal Reservoir. *PETRO: Jurnal Ilmiah Teknik Perminyakan, 11*(3), 138-148.

[16] Sutopo, Prabata, W., & Pratama, H. B. (2019). The development study of Karaha–Talaga Bodas geothermal field using numerical simulation.

Geothermal Energy, 7(1), 21. [CrossRef]

[17] Wang, M., Yang, F., Zhang, Y., Zhang, D., Feng, J., Luo, J., & Zeng, Y. (2022). Probabilistic geothermal resource assessment in Maichen Sag, south China. *Frontiers in Earth Science, 10*, 972125. [CrossRef]

[18] Ye, Z., Wang, J. G., & Yang, J. (2024). A Multi-objective Optimization Approach for a Fault Geothermal System Based on Response Surface Method. *Geothermics, 117*, 102887. [CrossRef]

[19] Kennedy, J., & Eberhart, R. (1995, November). Particle swarm optimization. In *Proceedings of ICNN'95-international conference on neural networks* (Vol. 4, pp. 1942-1948). IEEE. [CrossRef]

[20] Buster, G., Siratovich, P., Taverna, N., Rossol, M., Weers, J., Blair, A., ... & Akerley, J. (2021). A New Modeling Framework for Geothermal Operational Optimization with Machine Learning (GOOML). *Energies, 14*(20), 6852. [CrossRef]

[21] Bassam, A., Santoyo, E., Andaverde, J., Hernández, J. A., & Espinoza-Ojeda, O. M. (2010). Estimation of static formation temperatures in geothermal wells by using an artificial neural network approach. *Computers & Geosciences, 36*(9), 1191-1199. [CrossRef]

[22] Samnioti, A., & Gaganis, V. (2023). Applications of Machine Learning in Subsurface Reservoir Simulation–A Review–Part II. *Energies, 16*(18), 6727. [CrossRef]

[23] Myers, R. H., Montgomery, D. C., & Anderson-Cook, C. M. (2016). *Response surface methodology: process and product optimization using designed experiments*. John Wiley & Sons. [CrossRef]

[24] Quinao, J. J. D., & Zarrouk, S. J. (2018). Geothermal resource assessment using experimental design and response surface methods: The Ngatamariki geothermal field, New Zealand. *Renewable Energy, 116*, 324-334. [CrossRef]

[25] Jaber, A. K., Al-Jawad, S. N., & Alhuraishawy, A. K. (2019). A review of proxy modeling applications in numerical reservoir simulation. *Arabian Journal of Geosciences, 12*(22), 701. [CrossRef]

[26] Anifowose, F., Abdulraheem, A., & Al-Shuhail, A. (2019). A parametric study of machine learning techniques in petroleum reservoir permeability prediction by integrating seismic attributes and wireline data. *Journal of Petroleum Science and Engineering, 176*, 762-774. [CrossRef]

[27] Bergen, K. J., Johnson, P. A., de Hoop, M. V., & Beroza, G. C. (2019). Machine learning for data-driven discovery in solid Earth geoscience. *Science, 363*(6433), eaau0323. [CrossRef]

[28] Okoroafor, E. R., Smith, C. M., Ochie, K. I., Nwosu, C. J., Gudmundsdottir, H., & Aljubran, M. J. (2022). Machine learning in subsurface geothermal energy: Two decades in review. *Geothermics, 102*, 102401. [CrossRef]

[29] Sircar, A., Yadav, K., Rayavarapu, K., Bist, N., & Oza, H. (2021). Application of machine learning and artificial intelligence in oil and gas industry. *Petroleum Research, 6*(4), 379-391. [CrossRef]

[30] Ahmad, T., Zhang, D., Huang, C., Zhang, H., Dai, N., Song, Y., & Chen, H. (2021). Artificial intelligence in sustainable energy industry: Status quo, challenges and opportunities. *Journal of Cleaner Production, 289*, 125834. [CrossRef]

[31] Gudmundsdottir, H., & Horne, R. N. (2020, February). Prediction modeling for geothermal reservoirs using deep learning. In *45th workshop on geothermal reservoir engineering. Stanford, California: Stanford University* (pp. 1-12). https://pangea.stanford.edu/ERE/db/GeoConf/papers/SGW/2020/Gudmundsdottir.pdf

[32] Li, Y., Júlíusson, E., Pálsson, H., Stefánsson, H., & Valfells, Á. (2017). Machine Learning for Creation of Generalized Lumped Parameter Tank Models of Low Temperature Geothermal Reservoir Systems. *Geothermics, 70*, 62-84. [CrossRef]

[33] Duplyakin, D., Beckers, K. F., Siler, D. L., Martin, M. J., & Johnston, H. E. (2022). Modeling subsurface performance of a geothermal reservoir using machine learning. *Energies, 15*(3), 967. [CrossRef]

[34] Friedman, J. H. (2001). Greedy function approximation: A gradient boosting machine. *The Annals of Statistics, 29*(5), 1189. [CrossRef]

[35] Shahdi, A., Lee, S., Karpatne, A., & Nojabaei, B. (2021). Exploratory Analysis of Machine Learning Methods in Predicting Subsurface Temperature and Geothermal Gradient of Northeastern United States. *Geothermal Energy, 9*(1). [CrossRef]

[36] Al-Anazi, A. F., & Gates, I. D. (2010). Support vector regression for porosity prediction in a heterogeneous reservoir: A comparative study. *Computers & Geosciences, 36*(12), 1494-1503. [CrossRef]

[37] Chicco, D., Warrens, M. J., & Jurman, G. (2021). The coefficient of determination R-squared is more informative than SMAPE, MAE, MAPE, MSE and RMSE in regression analysis evaluation. *PeerJ Computer Science, 7*, e623. [CrossRef]

[38] Feng, J., Zhang, Y., He, Z., Gao, C., & Zhang, L. (2019, February). A Discussion of Methodology Study on Geothermal Reservoir Evaluating. In *Proceedings, 44th Workshop on Geothermal Reservoir Engineering* (pp. 1-7). https://pangea.stanford.edu/ERE/pdf/IGAstandard/SGW/2019/Feng.pdf

[39] Ciriaco, A. E., Zarrouk, S. J., & Zakeri, G. (2020). Geothermal resource and reserve assessment methodology: Overview, analysis and future directions. *Renewable and Sustainable Energy Reviews, 119*, 109515. [CrossRef]

[40] Holtzman, B. K., Paté, A., Paisley, J., Waldhauser, F., & Repetto, D. (2018). Machine learning reveals cyclic changes in seismic source spectra in Geysers geothermal field. *Science advances, 4*(5), eaao2929.

[CrossRef]

[41] Zheng, Y., Li, J., Lin, R., Hu, H., Gao, K., & Huang, L. (2021, February). Physics-guided machine learning approach to characterizing small-scale fractures in geothermal fields. In *Proceedings, forty-sixth workshop on geothermal reservoir engineering, Stanford University* (pp. 1-9). https://pangea.stanford.edu/ERE/db/GeoConf/papers/SGW/2021/Zheng.pdf

[42] Siler, D. L., Pepin, J. D., Vesselinov, V. V., Mudunuru, M. K., & Ahmmed, B. (2021). Machine learning to identify geologic factors associated with production in geothermal fields: a case-study using 3D geologic data, Brady geothermal field, Nevada. *Geothermal Energy, 9*(1), 17. [CrossRef]

[43] Tut Haklidir, F. S., & Haklidir, M. (2020). Prediction of Reservoir Temperatures Using Hydrogeochemical Data, Western Anatolia Geothermal Systems (Turkey): A Machine Learning Approach: Tut Haklidir and Haklidir. *Natural Resources Research, 29*(4), 2333-2346. [CrossRef]

[44] Shi, H., Zhang, Y., Cheng, Y., Guo, J., Zheng, J., Zhang, X., ... & Bai, L. (2025). A novel machine learning approach for reservoir temperature prediction. *Geothermics, 125*, 103204. [CrossRef]

Eric Thompson Brantson holds PhD in Petroleum and Natural Gas Engineering from China University of Geosciences, Beijing, China. He is currently a Senior lecturer and Head of Department at the Petroleum and Natural Gas Engineering Department at the University of Mines and Technology (UMaT), Tarkwa. Dr Brantson has a profound interest in Reservoir Modelling and Simulation, Enhanced Oil Recovery, Software Development in Petroleum Engineering, and Application and development of Artificial Intelligence Techniques in Petroleum. (Email: etbrantson@umat.edu.gh)

Stephen Dwamena Akoto Obeng holds a Bachelor of Science degree in Petroleum Engineering from the University of Mines and Technology (UMaT). His core technical interests lie in reservoir modelling and simulation, as well as the application of artificial intelligence and machine learning to solve energy industry challenges. (Email: stephenobeng6@gmail.com)

Daniel Ocran currently works at the Department of Petroleum and Natural Gas Engineering, University of Mines and Technology, Tarkwa-Ghana. His research interests include petroleum economics and petroleum upstream exploration policy analysis, oil and gas reservoir characterization and simulation, natural gas engineering, oil and gas production optimization, and applications of metaheuristic intelligent systems in optimal design of petroleum fiscal system. (Email: docran@umat.edu.gh)

Emmanuel Karikari Duodu is currently pursuing an M.Sc. in Petroleum and Natural Gas Engineering at the China University of Geosciences, Beijing, China. His academic research focuses on cutting-edge and sustainable energy technologies, with specialized interests in CO_2 capture, utilization and storage (CCUS), nanoparticles transport in enhanced oil recovery (EOR), artificial intelligence modelling for petroleum engineering applications, hydrogen storage and transportation, and the geomechanical properties of reservoirs. Mr. Duodu is dedicated to advancing the field of energy engineering through innovative research and data-driven solutions. (Email: emmanuel.duodu2018@gmail.com)

Zainab Ololade Iyiola, SPE, is a graduate student at the University of Oklahoma (OU), pursuing dual master's degrees in petroleum engineering and data science. She graduated top of her class from the University of Mines and Technology in Ghana and was selected as a delegate for the 2022 IPTC Education Week in Saudi Arabia. Her research focuses on hydrogen energy, carbon capture, storage, and utilization, enhanced oil recovery, and machine learning applications in energy. She is passionate about applying technology to solve real-world energy challenges. She is a recipient of several honors, including the 2024 Egbert Imomoh SPE Scholarship and the African Energy Chamber Scholarship. (Email: zainab.iyiola@ou.edu)

Eugene Jerry Adjei holds a BSc in Petroleum and Natural Gas Engineering from the University of Mines and Technology (UMaT), Tarkwa, Ghana. He has a keen interest in Modelling and Simulation, and Software Development in general. (Email: adjeieugenejerry@gmail.com)

Adu Gyamfi Owusu is currently pursuing an M.Sc in Petroleum Engineering at Nazarbayev University in Astana, Kazakhstan. His academic research focuses on the use of biosurfactants for enhanced oil recovery (EOR), modelling of fractured reservoirs, and drilling optimization. (Email: gyamfiadu511@gmail.com)